COLLISIONAL PARTICLE DISKS

YORAM LITHWICK[1] AND EUGENE CHIANG[2,3]

ABSTRACT

We present a new, simple, fast algorithm to numerically evolve disks of inelastically colliding particles surrounding a central star. Our algorithm adds negligible computational cost to the fastest existing collisionless N-body codes and can be used to simulate, for the first time, the interaction of planets with disks over many viscous times. Although the algorithm is implemented in two dimensions—i.e., the motions of bodies need only be tracked in a plane—it captures the behavior of fully three-dimensional disks in which collisions maintain inclinations that are comparable to random eccentricities. The method simulates vertically optically thin disks of identical collisional, massless, inelastic, indestructible test particles. We subject the algorithm to a battery of tests for the case of an isolated narrow circular ring. Numerical simulations agree with analytic theory with regard to how particles' random velocities equilibrate, how the ring viscously spreads, and how energy dissipation, angular momentum transport, and material transport are connected. We derive and measure the critical value of the coefficient of restitution, above which viscous stirring dominates inelastic damping and the particles' velocity dispersion runs away.

Subject headings: accretion, accretion disks — planets: rings

1. INTRODUCTION

How does a disk of collisional particles surrounding a star evolve in the presence of planets? The answer to this question has important implications. For example, after the planets of our solar system accreted most of their mass, many small rocky and icy bodies remained orbiting the Sun. Somehow the planets eliminated most of these remnant planetesimals, while leaving some behind to form the asteroid belt, the Kuiper Belt, and the Oort Cloud. In the vicinity of Uranus and Neptune, the small bodies must have been highly collisional. Otherwise these planets would have taken 10^{12} yr to form in situ (Thommes et al. 2003; Goldreich et al. 2004).[4] Yet virtually all simulations of the late stages of planet formation in the outer solar system—such as those that model the migration of the ice giants, the resulting trapping of Kuiper Belt objects into resonances, and the ejection of small bodies to the Oort Cloud—neglect collisions. When the effects of collisions are accounted for, the current picture of the formation of planetary systems may change drastically.

Planetary rings provide another setting in which interparticle collisions play a crucial role. What are the origins of narrow rings shepherded by satellites? How do narrow rings settle into their special apsis- and node-aligned states (e.g., Chiang & Culter 2004)? And how do rings back-react on and shape the orbits of shepherd satellites? Our understanding of satellite-ring interactions bears on mysteries such as the origin of the eccentricities of extrasolar giant planets (e.g., Goldreich & Sari 2003).

Despite its importance, the behavior of particle disks in the presence of perturbing bodies is poorly understood. Numerical simulations can help to further understanding. But until now, simulations of collisional disks have been too inefficient to follow, say, how disks viscously spread in the long term. Collisions are traditionally simulated with a brute-force method (e.g., Brahic 1977; Wisdom & Tremaine 1988): at each time step of the integration of the gravitational equations of motion it is determined which pairs of particles might collide before the next time step. These potential collision pairs are then integrated forward in time with a much smaller time step to see if they really do collide. But this method is inefficient: a brute-force search for collision partners requires around $N_{\rm tp}^2$ operations at each time step, where $N_{\rm tp}$ is the number of test particles. In addition, most potentially colliding pairs do not collide, particularly in optically thin disks. Hence, much computing time is wasted on missed collisions. More complex algorithms have been devised to reduce computing time (e.g., Lewis & Stewart 2000; Charnoz et al. 2001). But these are still not nearly as fast as the fastest collisionless N-body codes, such as SWIFT (Levison & Duncan 1994).

We sought a collision algorithm that (1) could be added to any N-body code, such as the freely available SWIFT; (2) contributes negligibly to the computational cost; (3) is simple conceptually; (4) is easy to code; and (5) follows correctly the long-term viscous evolution of disks in the presence of planets. We designed our algorithm to simulate a vertically optically thin disk of identical collisional, massless, inelastic but indestructible test particles that feel the gravity of the Sun and of multiple planets. Complications that we do not include, such as the self-gravity of the particles, order-unity optical depths, and particles with differing sizes, spins, and cohesive strengths, could all affect the viscous evolution in ways that are not currently understood. But at this stage it seems wisest to ignore these complications, even though the algorithm could be modified to handle them. Viewed in the most basic terms, inelastic collisions dampen random velocities and act as a source of friction between neighboring streamlines. As long as our algorithm preserves this behavior, while conserving angular momentum and accounting for the loss of energy in inelastic collisions, it seems likely that it will properly model the long-term evolution of collisional disks. In the present paper, we test this assertion thoroughly when there are no planets, comparing in detail the results of our simulations with those of analytic theory. In a future paper, we shall include planets.

2. THE COLLISION ALGORITHM

The gravitational equations for the motions of the Sun, planets, and massless test particles are integrated with the Wisdom-Holman

---

[1] Canadian Institute for Theoretical Astrophysics, Toronto, ON, Canada.
[2] Astronomy Department, University of California at Berkeley, CA.
[3] Alfred P. Sloan Research Fellow.
[4] In the terrestrial zone, the small bodies were also likely collisional, although the case is not as convincing there as it is in the outer solar system (Goldreich et al. 2004).

mapping method (Wisdom & Holman 1991), using the SWIFT subroutine package (Levison & Duncan 1994). All bodies are evolved in two dimensions: out-of-plane velocities and coordinates are always identically zero.

We supplement SWIFT with a subroutine that simulates collisions between test particles in a disk with vertical optical depth

$$\tau \sim N_{\text{tp}} \frac{s^2}{\bar{r}\Delta} < 1, \qquad (1)$$

where N_{tp} is the number of test particles, s is their size, and $\bar{r}$ and Δ are, respectively, the mean orbital radius and the radial width of the annulus that the particles occupy. In collisional particle disks, collisions tend to isotropize the velocity distribution.[5] The collision time is $t_{\text{col}} \sim 1/(n_v s^2 u)$, where u is the one-dimensional random speed and n_v is the volumetric number density, which is related to τ via $\tau \sim n_v s^2 u t_{\text{orb}}$. Therefore

$$t_{\text{col}} \sim \frac{t_{\text{orb}}}{\tau}. \qquad (2)$$

The collision time is longer than the orbital time by the u-independent factor $1/\tau$.

We capture this behavior with two-dimensional simulations in which all bodies have zero inclination. For every time step dt, a two-dimensional square grid is built, with each grid element having dimensions $s_{\text{grid}} \times s_{\text{grid}}$; here, s_{grid} can be thought of as the size of a particle. If two test particles fall in the same grid cell, and if their relative speed is negative (i.e., if they are approaching each other), then they collide with each other with probability $P_{\text{col}} = dt/t_{\text{orb}} \ll 1$, where t_{orb} is the orbital time at the collision point. A random number generator is used to determine whether or not they actually collide.

To see that this algorithm gives the same collision time as equation (2) (where τ is given by eq. [1] with $s \to s_{\text{grid}}$), it is instructive to consider first a simpler algorithm that also yields the correct collision time. In this simpler algorithm, one waits for a time interval of t_{orb} (instead of dt) before finding which particles fall in the same grid cell. Then two particles that do fall in the same grid cell, and have converging velocities, collide with probability $P_{\text{col}} = 1$. Since the probability that a given particle lies in a cell occupied by a second particle is τ, the collision time is t_{orb}/τ, as required.[6] Turning now to the algorithm that we actually use, since we apply this algorithm every time interval dt (and not t_{orb}), we must correspondingly reduce the probability of a collision by dt/t_{orb} in order to maintain the collision time at the value given by equation (2).

Although carried out in only two dimensions, we emphasize that our algorithm models three-dimensional disks in which collisions maintain inclinations that are comparable to the random eccentricities. A truly two-dimensional disk is not realistic, because collisions invariably generate out-of-plane velocities. But if one could somehow prevent the generation of out-of-plane velocities, the collision time in such a disk would be $\sim s/(u\tau)$, which differs from equation (2) by the factor $s/(ut_{\text{orb}})$. Since our algorithm satisfies equation (2), it does not model truly two-dimensional disks.

As will be shown below, collisions drive the random speed of the particles to $u \gtrsim s_{\text{grid}}/t_{\text{orb}}$. Hence, if two particles fall in the same grid cell at one time, they will usually fall in separate grid cells after one orbital period. Since collisions can potentially occur every time step, it might be thought that the same two particles can collide many times in succession—a behavior that we consider undesirable. But this behavior is avoided by the requirement that particles must be approaching each other for a collision to occur; immediately after they collide, their relative velocities reverse signs, and they are no longer candidates for a collision pair.

One of the main advantages of our algorithm is that the time step is not restricted by the Courant condition. In a naive brute-force algorithm, one must restrict $dt \ll s/u$ in order to ensure that any two particles that fall within a distance s of each other collide. This restriction on dt can be very cumbersome when $u \gg s/t_{\text{orb}}$, as it will be whenever planets stir up the eccentricities. We avoid the Courant condition by treating the vertical dimension statistically: when two particles fall within the same two-dimensional grid cell, they need only collide a small fraction of the time because their vertical positions will, in general, differ. With our algorithm, we may choose dt to be as large as is allowed by SWIFT, which is typically a significant fraction of the orbital time.

If two particles have been selected for a collision, i.e., if they lie in the same grid cell, are approaching each other, and are selected by the random number generator, then their velocities are updated as though the bodies were frictionless spheres whose surfaces touch (e.g., Trulsen 1971): the component of the relative velocity vector that lies parallel to the axis connecting the two particles is reversed in sign (from a converging velocity to a diverging one) and multiplied by the coefficient of restitution ϵ, i.e., in obvious notation,

$$u'_{\text{rel},\parallel} = -\epsilon u_{\text{rel},\parallel}. \qquad (3)$$

Neither the perpendicular component of the relative velocity vector, nor the velocity of the center of mass of the two colliders, nor the positions of the colliders are changed by the collision. A collision does not alter the sum of the angular momenta of both colliding bodies; hence the collision algorithm exactly conserves total angular momentum. Note that a collision between two particles separated by distance d changes the velocities of the particles as though each were a smooth sphere with radius $d/2$. Since d changes from collision to collision, the particles' sizes are effectively changing; they are only approximately s_{grid}.[7]

The algorithm has now been completely described, aside from how the code finds which pairs of particles lie in the same grid cell. To find colliding pairs, the code first determines in which grid cell each particle lies. A grid cell is labeled by two integers representing its location along the x- and y-axes. Second, the code sorts the grid cells that contain test particles with the heapsort algorithm (Press et al. 1992). The sorted occupied grid cells are then checked to see if the same grid cell is repeated for two different particles. The step that takes the most time in the entire collision algorithm is the heapsort, which requires $\sim N_{\text{tp}} \ln N_{\text{tp}}$ operations. However, in the runs presented in this paper, with

---

[5] More precisely, in optically thin disks the rms azimuthal speed is twice the rms radial speed; the rms vertical speed is comparable.

[6] Although this simpler algorithm yields the correct collision time, we did not use it, because it introduces an artificial frequency into the problem, set by the time interval at which the algorithm is applied ($\sim t_{\text{orb}}$). When we attempted this algorithm, we found that a gap was cleared in the disk of test particles where the orbital period was exactly equal to this interval.

[7] The effective vertical (out of plane) size of the particles is also $\sim s_{\text{grid}}$. It might be thought that, when $u \gg s_{\text{grid}}/t_{\text{orb}}$, the effective vertical size of the particles would be $\sim ut_{\text{orb}}$ (the scale height of the disk) since our algorithm effectively projects particles onto the midplane. But with our statistical treatment of the vertical dimension, particles that lie in the same two-dimensional grid cell do not always collide. The probability that they collide is chosen to keep the collision time $\sim t_{\text{orb}}/\tau$, as it would be for three-dimensional particles of size s_{grid}.
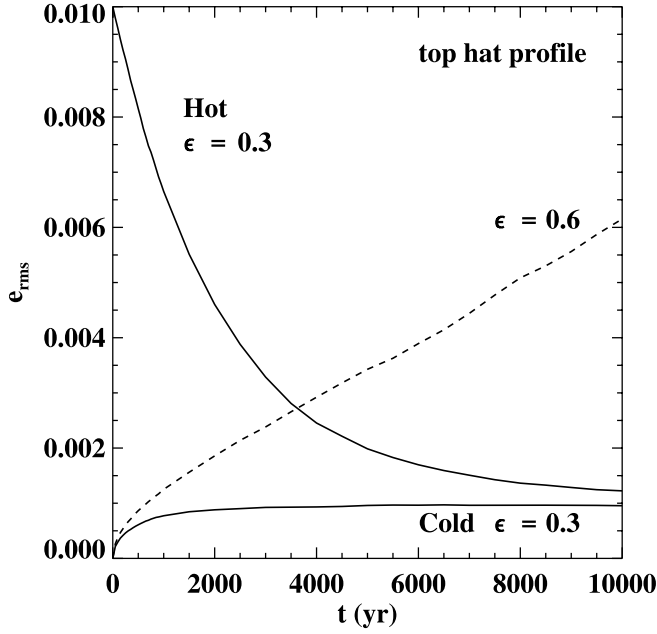
FIG. 1.—Random velocity evolution. The two simulations with $\epsilon = 0.3$ both relax to the same $e_{rms} \sim s_{grid}/\bar{r}$. In the $\epsilon = 0.6$ simulation, heating proceeds indefinitely.

$N_{tp} = 10^4$ particles, it was found that the collision algorithm contributed negligibly to the running time of SWIFT. For example, the run in Figure 1 labeled "Cold $\epsilon = 0.3$" took 623 s on a 2.5 GHz PowerPC G5. When the collision routine was turned off, the equivalent run took 475 s.

3. SIMULATIONS OF NARROW CIRCULAR RINGS

In the remainder of this paper, we investigate circular rings of particles without any planets. Circular rings are understood quite well theoretically (e.g., Lynden-Bell & Pringle 1974; Brahic 1977; Goldreich & Tremaine 1978; Shukhman 1984; Petit & Henon 1987). Our goal is not only to test the collision algorithm but also to develop diagnostics that can be used for the much more complicated case when planets are present.

The parameters of the simulation include the coefficient of restitution (ϵ), the size of a grid element (s_{grid}), the number of test particles (N_{tp}), and the initial orbital elements of the test particles. The central body's mass is $1\,M_\odot$. We simulate narrow rings with mean radius $\bar{r} = 1$ AU and radial width $\Delta \ll \bar{r}$, and choose $dt = 0.18$ yr for the integration time step.

A particle ring has two characteristic timescales (Brahic 1977). The shorter one is t_{col}, the time for a particle to collide. The longer one is t_{diff}, the time for particles to diffuse across the ring's width. Random velocities relax to their equilibrium distribution on timescale t_{col}, while the ring density evolves on timescale t_{diff}. We investigate in turn the evolution of random velocities and of density.

4. RANDOM VELOCITY EVOLUTION

4.1. Theory

Collisions can both excite random velocities by drawing energy from the background Keplerian shear ("viscous stirring") and damp random velocities because of finite inelasticity. When the coefficient of restitution $\epsilon < \epsilon_*$, where ϵ_* is a critical value, a typical collision damps random velocities. But there is a limit to how cold the particles get. Particles on circular orbits collide

with one another at the Keplerian shearing speed $\sim s\Omega$, where s is the size of a particle and Ω is the orbital angular frequency. In our collision routine, this relative speed is $\sim s_{grid}\Omega$. Since a single such collision redirects the particles onto noncircular orbits, the random velocity cannot fall below $\sim s_{grid}\Omega$ and the rms eccentricity always relaxes to

$$e_{rms} \sim \frac{s_{grid}}{r} \qquad (4)$$

in the $\epsilon \ll \epsilon_*$ limit, where r is the local disk radius. By contrast, when $\epsilon > \epsilon_*$, a typical collision excites random velocities: viscous stirring dominates inelastic damping, and the rms eccentricity runs away.

In optically thin disks composed of equal-size particles, ϵ_* is determined solely by the angular dependence of the differential collisional cross section. For frictionless spheres, $\epsilon_* = 0.63$ (Goldreich & Tremaine 1978). For frictional spinning spheres, $\epsilon_* = 0.92$ (Shukhman 1984). Since our algorithm only uses the two-dimensional cross section, whereas these authors use a three-dimensional cross section, it is to be expected that our ϵ_* will differ from these values. We defer the calculation of our ϵ_* to § 6.3.2, where we derive $\epsilon_* = \sqrt{7}/5 = 0.529$ (eq. [68]).

4.2. Simulations: Approach to Velocity Equilibrium

Figure 1 shows the time evolution of the rms eccentricity,

$$e_{rms} \equiv \left\langle e^2 \right\rangle^{1/2}, \qquad (5)$$

in three simulations, where $\langle \rangle$ averages over all test particles. In each simulation, $s_{grid} = 10^{-3}$ AU and $N_{tp} = 10^4$. Particles were initially on orbits evenly spaced in semimajor axis between $\bar{r} - \Delta_0/2$ and $\bar{r} + \Delta_0/2$, where $\bar{r} = 1$ AU and $\Delta_0 = 0.08$ AU (top-hat profile). Initial eccentricities were identical, and initial longitudes and pericenter longitudes were random.

Two simulations had $\epsilon = 0.3$. One of these was initially cold, with initial eccentricities $= 0$; the other was initially hot, with eccentricities $= 0.01$. In both simulations, e_{rms} approached $\sim s_{grid}/\bar{r} = 10^{-3}$ (eq. [4]). Clearly, inelastic damping dominates viscous stirring when $\epsilon = 0.3$. The third simulation had $\epsilon = 0.6$ and was initially cold. Its e_{rms} grew indefinitely. Hence, viscous stirring dominates when $\epsilon = 0.6$.

We define the collision time as

$$t_{col} \equiv \frac{N_{tp}/2}{\text{No. collisions per unit time}}. \qquad (6)$$

In the three simulations, we measured $t_{col} = 106$–108 yr. An estimation of t_{col} from the input parameters of a simulation follows from a more precise form of equations (1)–(2):

$$t_{col}^{(est)} = t_{orb} \frac{4\pi r}{n s_{grid}^2}, \qquad (7)$$

where

$$n \equiv dN_{tp}/dr \qquad (8)$$

is the number of particles per radial distance, and 4π is the product of two factors: 2π for the area of a ringlet ($2\pi r \times dr$), and 2 because only half of the time, when the relative velocity is negative, do doubly occupied grid cells lead to collisions. For the parameters of the present simulations, with $r = \bar{r}$ and $dN_{tp}/dr = N_{tp}/\Delta_0$, $t_{col}^{(est)} = 101$ yr. Because $t_{col}^{(est)}$ does not account for the
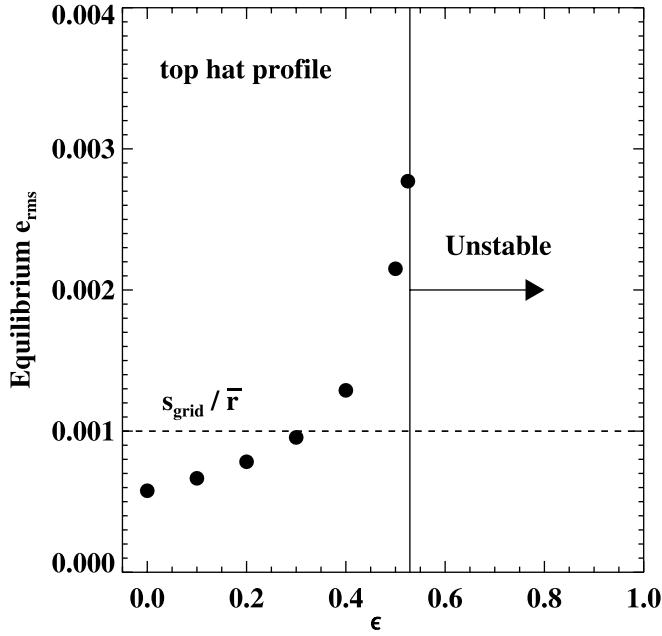
Fig. 2.—Equilibrium e_{rms}. The seven points denote the steady-state e_{rms} in simulations with differing ϵ. The vertical line shows the critical value $\epsilon_* = \sqrt{7}/5 = 0.529$. In initially cold simulations with $\epsilon = \{0, 0.1, 0.2, 0.3\}$, e_{rms} was evaluated at 10^4 yr. In initially cold simulations with $\epsilon = \{0.4, 0.5, 0.525\}$, e_{rms} was evaluated at 2×10^4 yr, since these simulations took longer to reach a steady state.

decreased collision frequency of particles at the edge of the ring, it underestimates t_{col} by a small amount. That t_{col} remained nearly constant throughout the simulation reflects the near constancy of the ring's width, since parameters were deliberately chosen to freeze out diffusion (from eq. [9] below, the diffusion time in these simulations is $\sim 10^5$ yr).

In the cold $\epsilon = 0.3$ simulation, e_{rms} reached 80% of its final value by time $t = 1000$ yr—around 10 collision times. The hot $\epsilon = 0.3$ simulation took much longer to reach velocity equilibrium: initially, e_{rms} decayed approximately exponentially with a time constant of 2500 yr—around 25 collision times. Even after $t = 2500$ yr, the hot simulation took hundreds of collision times to reach its final e_{rms}. Velocity equilibration in the hot simulation was so long because of particles at the ring edges. Edge particles tend to retain their initial eccentricities because their epicyclic excursions carry them away from the majority of particles; consequently, edge particles collide less frequently than do particles in the ring proper.

4.3. Simulations: Equilibrium Eccentricities

Figure 2 shows results from seven simulations, all with the same initial conditions as the cold simulations described in the previous subsection, except with differing values of ϵ. The seven plotted simulations, with $\epsilon \le 0.525$, all reached velocity equilibrium, with $e_{rms} \sim$ (order unity constant)$s_{grid}/\bar{r}$. Simulations with $\epsilon \ge 0.6$ never reached velocity equilibrium. We conclude that $0.525 < \epsilon_* < 0.6$ for our collisional cross section. In equation (68) below, we derive $\epsilon_* = \sqrt{7}/5 = 0.529$.

5. DENSITY EVOLUTION

5.1. Theory

A ring diffuses in the time that it takes a particle to random walk across its width. This random walk has a step-size equal to the epicyclic excursion of a particle ($\sim r e_{rms} \sim s_{grid}$) and a time

per random step of t_{col}. Thus, to diffuse the width of the ring Δ takes a time

$$t_{diff} \sim t_{col} \left(\frac{\Delta}{s_{grid}} \right)^2 \gg t_{col}, \qquad (9)$$

where the inequality holds when $\Delta \gg s_{grid}$; otherwise, $t_{diff} \sim t_{col}$ until $\Delta \sim s_{grid}$. Since $t_{col} \propto 1/n \propto \Delta$ (eq. [7]), a ring expands as

$$\Delta \propto t^{1/3}. \qquad (10)$$

More precisely, n satisfies the diffusion equation

$$\frac{\partial n}{\partial t} = \frac{\partial}{\partial r} \left(\nu \frac{\partial n}{\partial r} \right), \qquad (11)$$

where the viscosity $\nu = (\text{const})s_{grid}^2/t_{col}$ (eq. [9]). Inserting equation (7) into our expression for ν, we see that

$$\nu = k_\nu \frac{s_{grid}^4}{\bar{r} t_{orb}} n, \qquad (12)$$

which defines the dimensionless constant k_ν; k_ν is a function of ϵ, but is independent of s_{grid}, $\bar{r}$, and n. Petit & Henon (1987) derived the above diffusion equation and gave its self-similar solution, an expanding inverted parabola:

$$n = \frac{3}{2} \frac{N_{tp}}{\Delta} \left[1 - \left(\frac{r - \bar{r}}{\Delta/2} \right)^2 \right], \quad |r - \bar{r}| \le \Delta/2, \qquad (13)$$

where

$$\Delta \equiv \left(36 k_\nu \frac{s_{grid}^4}{\bar{r} t_{orb}} N_{tp} t \right)^{1/3}. \qquad (14)$$

Since the viscosity ν decreases with decreasing n, the diffusion is nonlinear and the edges of the ring at $r = \bar{r} \pm \Delta/2$ are sharp.

5.2. Simulations

Because of the steep dependence of the diffusion timescale on the width of the ring, $t \propto \Delta^3$, it takes a long time to simulate even a modest increase in Δ. Simulation parameters must be chosen judiciously. We fix $N_{tp} = 10^4$ and $\bar{r} = 1$ AU, and seek the optimal values for s_{grid} and $\Delta_0 \equiv \Delta|_{t=0}$. To simulate as large an increase in Δ as possible, the simulation should begin with as narrow a ring as possible. For a fixed s_{grid}, the narrowest ring that is not optically thick has unity optical depth $\Delta_0 \sim N_{tp}(s_{grid})^2/2\pi\bar{r}$. The evolution timescale at the start of the simulation is $t_0 = (\text{const})(\Delta_0)^3/(s_{grid})^4$ (eq. [14]), so with unity optical depth $t_0 = (\text{const})\Delta_0$. Hence, the fastest timescale is obtained with the smallest Δ_0. But we must have $\Delta_0 \ge s_{grid}$, so the optimal values are $\Delta_0 = s_{grid} = 2\pi\bar{r}/N_{tp}$. Rounding up, we set $\Delta_0 = s_{grid} = 10^{-3}$ AU.

Figures 3 and 4 portray results from a simulation with the parameters listed above and $\epsilon = 0.3$. Initially, the ring particles were uniformly distributed in a ring with edges at $1 \pm (5 \times 10^{-4})$ AU. In Figure 3, we show how the particles' dispersion in r,

$$\sigma_r \equiv \left\langle (r - \bar{r})^2 \right\rangle^{1/2}, \qquad (15)$$

and the collision time, t_{col}, vary with time, according to both theory and simulation. Figure 4 displays comparisons between
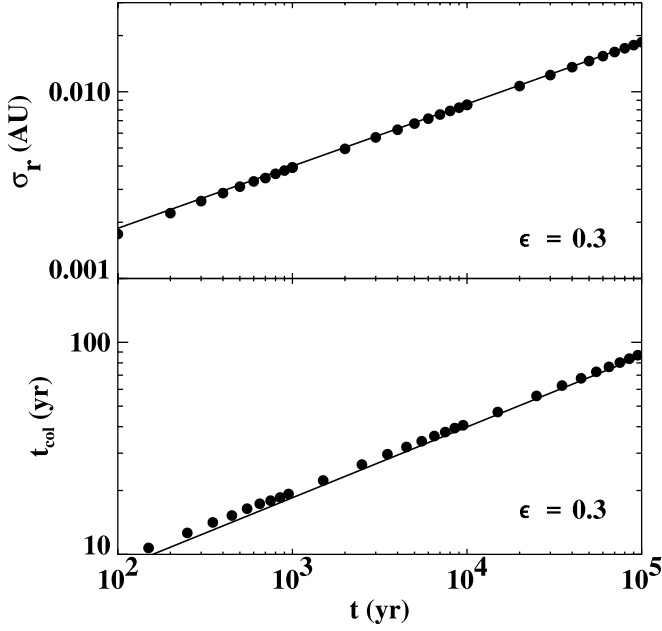
FIG. 3.—Dispersion and collision rate evolution in a diffusing ring. *Top panel*: Points show $\sigma_r = \langle (r - \bar{r})^2 \rangle^{1/2}$ from the numerical simulation. The theory line through the points is $\Delta/\sqrt{20}$ (eq. [16]), where Δ is given by eq. (14). The normalization of the line was adjusted by choosing $k_\nu = 0.016$. *Bottom panel*: Points show the collision time t_{col} from the simulation (eq. [6]). The theory line is given by eq. (17), with $k_\nu = 0.016$. Theory underestimates t_{col} by a small amount because of particles at the ring edges (§ 4.2).

theory and simulation for n. According to the theory described in § 5.1, $n(r)$ is given by equation (13), the dispersion in r is

$$\sigma_r^2 = \int (n/N_{tp})(r - \bar{r})^2 \, dr = \Delta^2/20, \qquad (16)$$

with Δ given by equation (14), and the collision time is

$$t_{col} = \left(\int \frac{1}{N_{tp}} \frac{n}{t_{col}^{(est)}} \, dr \right)^{-1} = 120\pi k_\nu \frac{(s_{grid})^2}{\Delta^2} t. \qquad (17)$$

The theory fits the numerical results well when we set

$$k_\nu = 0.016. \qquad (18)$$

6. ANGULAR MOMENTUM AND ENERGY TRANSPORT

Understanding how planets interact with disks requires understanding how angular momentum and energy are transported, both within disks and between planets and disks. Below we study transport in isolated, circular, narrow rings, developing diagnostics that will prove useful in future simulations of disks with planets.

6.1. Theory

The azimuthally averaged equations describing the conservation of particle number, angular momentum, and energy are

$$\partial_t n + \partial_r F_n = 0, \qquad (19)$$

$$\partial_t(Hn) + \partial_r(HF_n) = -\partial_r F_H^{visc}, \qquad (20)$$

$$\partial_t(En) + \partial_r(EF_n) = -\partial_r F_E^{visc} - n\dot{\mathcal{E}}, \qquad (21)$$

where F_n is the (net) number flux across a circle of radius r, i.e., the number of particles per unit time that exit this circle minus
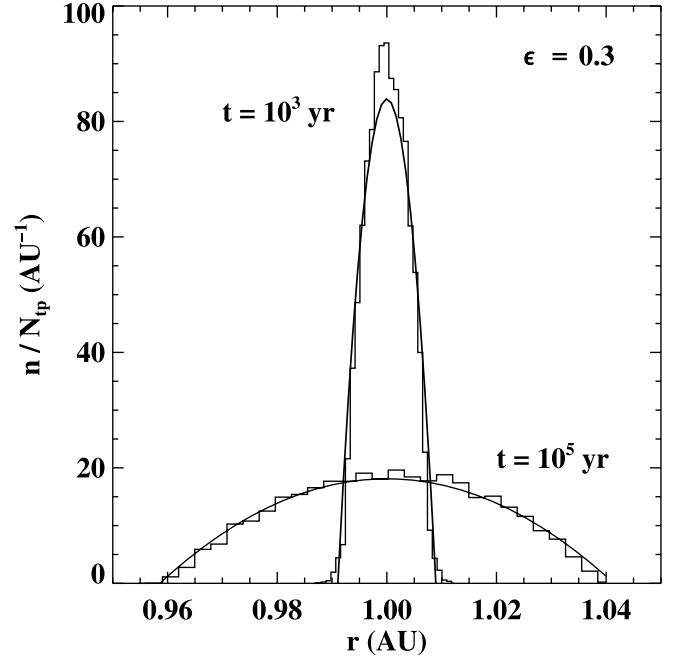

FIG. 4.—Density evolution in a diffusing ring. Histograms of the number density are shown at two times from the same simulation as in Fig. 3. The theory lines through the histograms are given by eq. (13), with k_ν the same as in Fig. 3.

the number that enter it; $H(r) \equiv (GM_\odot r)^{1/2}$ is the specific angular momentum of a particle on a circular orbit; $E(r) \equiv -GM_\odot/2r$ is the specific energy; F_H^{visc} (the "viscous flux of angular momentum") is defined as the difference between the total angular momentum flux and HF_n, i.e., $F_H^{visc} + HF_n = F_H^{tot}$; F_E^{visc} is the corresponding difference in energy fluxes, i.e., $F_E^{visc} + EF_n = F_E^{tot}$; and $\dot{\mathcal{E}}$ is the rate at which specific energy is lost, per particle, in inelastic collisions.

Our decomposition of F_H^{tot} into two components has the following interpretation: HF_n is the angular momentum flux that would be carried by particles on circular orbits whose radii change on timescales that are long compared to the orbit time, while F_H^{visc} is the part of the angular momentum flux not associated with the direct advection of circular orbits. The viscous flux of angular momentum and the corresponding viscous flux of energy are transferred in the ratio appropriate for circular orbits; i.e., since circular orbits have $E = -(1/2)(GM_\odot/H)^2$, a transfer in angular momentum of δH must be accompanied by a transfer in energy of $\delta E = (GM_\odot)^2 \delta H/H^3 = \Omega \delta H$, so

$$\frac{F_E^{visc}}{F_H^{visc}} = \Omega(r). \qquad (22)$$

The above relation applies only to the viscous fluxes, not to the total fluxes (i.e., $EF_n/HF_n = -\Omega/2$). Equations (20) and (21) simplify with the aid of equations (19) and (22) to

$$F_n = -\frac{2}{r\Omega} \partial_r F_H^{visc}, \qquad (23)$$

$$F_H^{visc} = -n\dot{\mathcal{E}}/(d\Omega/dr). \qquad (24)$$

The latter is the well-known relation between energy dissipation and viscous angular momentum flux for accretion disks (e.g., Lynden-Bell & Pringle 1974).

Since $\dot{\mathcal{E}} \sim s_{\text{grid}}^2 \Omega^2 / t_{\text{col}} \sim n s_{\text{grid}}^4 \Omega^2 / 4\pi r t_{\text{orb}}$, we may rewrite equation (19), using equations (23) and (24), as

$$\partial_t n = \left(\frac{k_E s_{\text{grid}}^4}{2 r t_{\text{orb}}} \right) \partial_r^2 n^2,$$ (25)

where

$$k_E \equiv \frac{n\dot{\mathcal{E}}}{n^2 s_{\text{grid}}^4 \left(3\Omega^2 / 8 r t_{\text{orb}} \right)}$$ (26)

is an ϵ-dependent dimensionless constant. In deriving equation (25), we have dropped terms that are small for narrow rings [e.g., $|d(\ln \Omega)/dr| \ll |d(\ln n^2)/dr|$]. Equation (25) is identical to equations (11)–(12) provided $k_E = k_\nu$.

6.2. *Simulations*

In this subsection, we diagnose angular momentum and energy transport in numerical simulations and compare to theory. To measure the number flux F_n across a circle of radius r, we evaluate $N_{>r}$, the number of particles whose radial distances from the Sun exceed r, at two times, t_m and $t_m + dt_m$. Then

$$F_n(r, t_m) \doteq \frac{N_{>r}(t_m + dt_m) - N_{>r}(t_m)}{dt_m},$$ (27)

where the symbol $\doteq$ means that this is how F_n is measured. Similarly, we measure the total angular momentum flux as

$$F_H^{\text{tot}}(r, t_m) \doteq \frac{H_{>r}(t_m + dt_m) - H_{>r}(t_m)}{dt_m},$$ (28)

where $H_{>r}$ is the sum of the specific angular momenta of all particles whose radial distances exceed r. For the energy flux, we must account for the energy lost in inelastic collisions (where the specific energy lost per collision $= u_{\text{rel},\|}^2 (1 - \epsilon^2)/4$; see eq. [3]). To this end, when calculating the energy flux across a circle with radius r, we first calculate $\delta\mathcal{E}_{>r}$, the total specific energy lost between times t_m and $t_m + dt_m$ in all inelastic collisions that occurred at radii $>r$. Then the total energy flux is

$$F_E^{\text{tot}}(r, t_m) \doteq \frac{E_{>r}(t_m + dt_m) - E_{>r}(t_m) + \delta\mathcal{E}_{>r}}{dt_m},$$ (29)

where $E_{>r}$ is the sum of the specific energies of particles with radii greater than r. The viscous fluxes are determined by the three fluxes above:

$$F_H^{\text{visc}} \doteq F_H^{\text{tot}} - HF_n,$$ (30)
$$F_E^{\text{visc}} \doteq F_E^{\text{tot}} - EF_n.$$ (31)

Energy dissipation in an annulus between radius r_1 and r_2 is measured via

$$n\dot{\mathcal{E}} \doteq \frac{\delta\mathcal{E}_{>r_1} - \delta\mathcal{E}_{>r_2}}{(r_2 - r_1) dt_m}.$$ (32)

Figure 5 shows a number of measurements of the angular momentum flux for the simulation whose parameters are given in § 5.2. The theory curve is from equations (24) and (26):

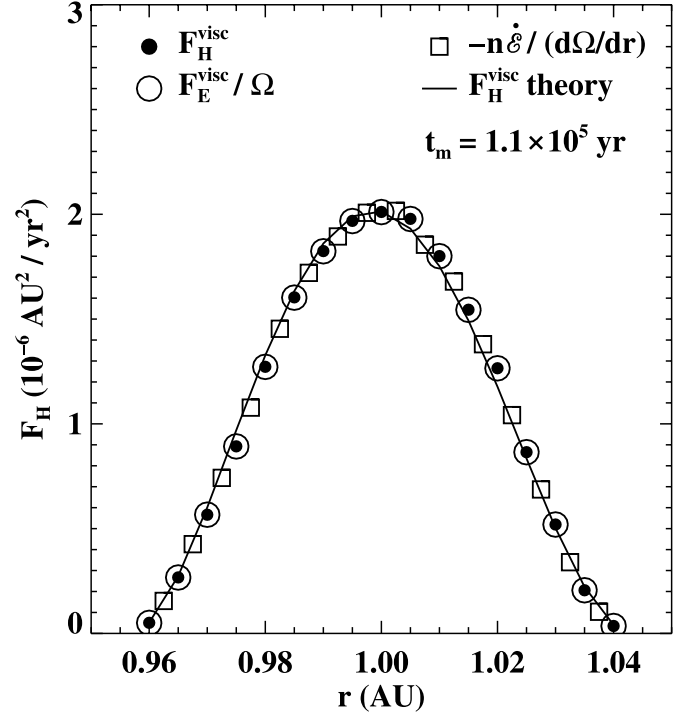$$F_H^{\text{visc}} = k_E \frac{n^2 s_{\text{grid}}^4 \Omega}{4 t_{\text{orb}}},$$ (33)

FIG. 5.—Angular momentum flux measured with various methods. Data are taken from the simulation described in § 5.2 (Figs. 3–4) at time $t_m = 1.1 \times 10^5$ yr, with measurement interval $dt_m = 10^4$ yr. The theory line is eq. (33). F_H^{visc} is measured with eq. (30). F_E^{visc} is measured with eq. (31); clearly $F_E^{\text{visc}}/\Omega = F_H^{\text{visc}}$, confirming eq. (22). $n\dot{\mathcal{E}}$ is measured with eq. (32); the squares confirm eq. (24).

with n given by equation (13) and $k_E = k_\nu = 0.016$ (we verify the equality of k_E and k_ν in Fig. 7 below). Overlaid on this theory curve are three sets of data points measured in three independent ways. The agreement between theory and simulations is excellent.

Figure 6 shows the number fluxes for the same simulation. The theory line shows (eqs. [23] and [33])

$$F_n = -k_E \frac{s_{\text{grid}}^4}{2\bar{r} t_{\text{orb}}} \frac{\partial n^2}{\partial r},$$ (34)

with n from equation (13). The data points agree well with the theory, although there is some scatter.

The circles in Figure 7 show the energy dissipation constant k_E (eq. [26]) for the simulations described in §§ 4.2–4.3 at the same output times (Fig. 2). Recall that each of these simulations has a top-hat density profile and is run for much less than a viscous time, so the density hardly evolves. The simulation with $\epsilon = 0.3$ has $k_E = 0.016$. Therefore $k_E = k_\nu$ (eq. [18]), as suggested below equation (26). Note that it is much more efficient to measure k_E than k_ν, since k_E can be measured in only a few collision times, whereas k_ν must be measured on the viscous timescale. We defer to § 6.4 a discussion of the diamonds and stars in Figure 7.

6.3. *Dynamics from a Microscopic Perspective: Theory*

The angular momentum flux advected by particles is

$$n\langle r(\Omega r + v_\phi)v_r \rangle = HF_n + nr\langle v_r v_\phi \rangle,$$ (35)

where $\boldsymbol{v} = (v_r, v_\phi)$ is the difference between a particle's total velocity (in the radial r and azimuthal ϕ directions) and the Keplerian circular velocity at its position, and $\langle \; \rangle$ denotes an average over particles in a narrow ring. Defining

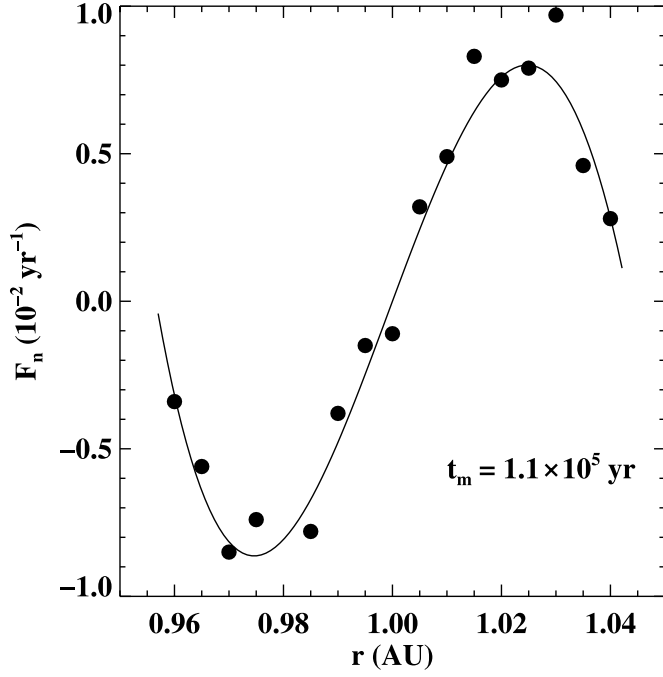$$F_{r\phi} \equiv nr\langle v_r v_\phi \rangle,$$ (36)

FIG. 6.—Number flux. Data are taken from the same simulation as in Fig. 5 and at the same times. The theory line is eq. (34). Data points are measured with eq. (27).

we have

$$F_H^{\text{tot}} = HF_n + F_{r\phi} + F_{\text{NL}}, \qquad (37)$$

where F_{NL} is the "nonlocal" flux, i.e., the angular momentum flux not advected by particles (Wisdom & Tremaine 1988). In § 6.1, we considered only the combination

$$F_H^{\text{visc}} = F_{r\phi} + F_{\text{NL}}. \qquad (38)$$

In this subsection, we wish to calculate F_H^{visc} in terms of microscopic quantities. Hence we must consider the two components of F_H^{visc} separately. The two components have the following interpretation: (1) a particle that crosses a circle of radius r has an angular momentum H' that is not, in general, equal to $H(r)$; the difference $H' - H(r)$ contributes to $F_{r\phi}$. (2) When a particle that is inside of the circle collides with one that is outside, the angular momentum transferred across the circle contributes to F_{NL}.

For a collisionless Keplerian particle, to lowest order in e,

$$v_r = er\Omega \sin(\Omega t), \qquad (39)$$

$$v_\phi = \frac{1}{2} er\Omega \cos(\Omega t), \qquad (40)$$

with r and Ω independent of time. Therefore, for collisionless particles, $F_{r\phi} \propto \langle v_r v_\phi \rangle \propto \langle \sin(2\Omega t)\rangle = 0$. But collisions give a definite contribution to $\langle v_r v_\phi \rangle$ (Greenberg 1988), as we presently show.

Instead of averaging over space only (as denoted by $\langle v_r v_\phi \rangle$), it will prove convenient to average over both space and time. We average over a radial width Δr that is larger than the particle size but smaller than the scale length over which the density varies. We also average over a time Δt that is longer than a few collision times but shorter than the timescale over which the density changes. The average $\overline{F}_{r\phi}$ is defined via

$$(\Delta t \Delta r)\overline{F}_{r\phi} \equiv \int_t^{t+\Delta t} \int_r^{r+\Delta r} dt'\, dr'\left(nr'v_r v_\phi\right), \qquad (41)$$
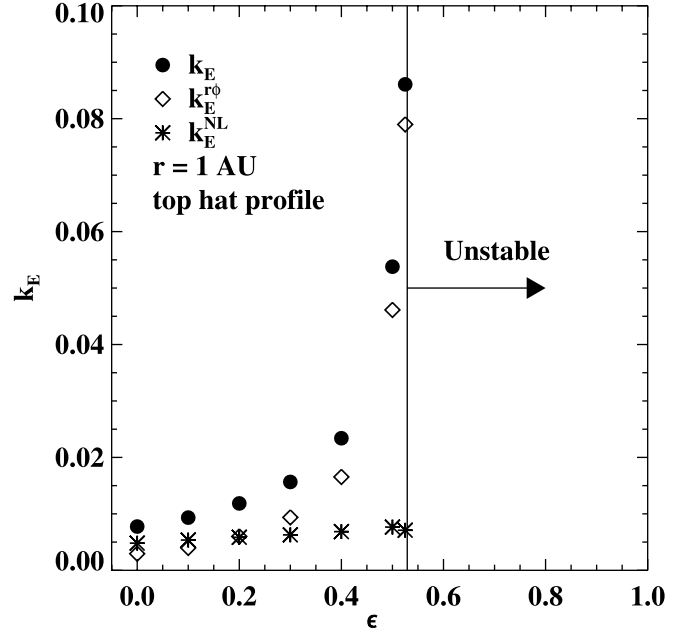

FIG. 7.—Energy dissipation. The simulations are the same as those described in Fig. 2. Circles show k_E, measured with eqs. (26) and (32). Measurement parameters include $r_1 = 0.99$ AU, $r_2 = 1.01$ AU, and $dt_m = 5000$ yr, with $t_m = 5000$ yr for $\epsilon = \{0, 0.1, 0.2, 0.3\}$ and $t_m = 15{,}000$ yr for $\epsilon = \{0.4, 0.5, 0.525\}$. For $\epsilon = 0.3$, $k_E = 0.016$, a value that matches k_ν as given by eq. (18). Diamonds show $k_E^{r\phi} \propto F_{r\phi}$, measured as described in § 6.4. Stars give $k_E^{\text{NL}} = k_E - k_E^{r\phi} \propto F_{\text{NL}}$; this quantity is practically constant with ϵ, as expected from eq. (51). Most of the energy dissipation (viscous transport of angular momentum) arises from $F_{r\phi}$ and not from F_{NL} as ϵ approaches ϵ_*; compare with eqs. (50)–(51).

where $\boldsymbol{v}$ is a Lagrangian quantity that is tied to particles. Extracting $F_{r\phi}$ from a numerical simulation with only a spatial average ($\langle v_r v_\phi \rangle$) can lead to large errors. In particular, in an optically thin disk, only a small fraction of the particles have collided within the last orbital period. Hence, most particles contribute negligibly to $\langle v_r v_\phi \rangle$, and a calculation of $\langle v_r v_\phi \rangle$ can become plagued by small-number statistics.

For a single particle that does not collide in the interval Δt,

$$\int_t^{t+\Delta t} v_r v_\phi\, dt' = -\Omega^{-1}\int \frac{dv_\phi^2}{dt}\, dt = -\Omega^{-1}\left(v_\phi^2|_{t+\Delta t} - v_\phi^2|_t\right). \qquad (42)$$

But if it collided once,

$$\int_t^{t+\Delta t} v_r v_\phi\, dt' = -\Omega^{-1}\left(v_\phi^2|_{t+\Delta t} - v_\phi^2|_t - \delta(v_\phi^2)\right), \qquad (43)$$

where δ represents the change due to the collision. Therefore each collision contributes to equation (41) in the amount of

$$(\Delta t \Delta r)\delta\overline{F}_{r\phi} = r\Omega^{-1}\left(\delta\left(v_{\phi,1}^2\right) + \delta\left(v_{\phi,2}^2\right)\right), \qquad (44)$$

where $\delta(v_{\phi,1}^2)$ and $\delta(v_{\phi,2}^2)$ are the contributions from the two collision partners. The contribution from the endpoints, $v_\phi^2|_{t+\Delta t} - v_\phi^2|_t$, can be neglected as long as Δt is much longer than the collision time.

We define

$$(\Delta t \Delta r)\overline{F}_{\text{NL}} \equiv \int\int dt'\, dr' F_{\text{NL}}. \qquad (45)$$

If two particles collide when their positions are at radii r_1 and r_2 (where $r < r_2 < r_1 < r + \Delta r$), and if the particle at r_1 has its ϕ-velocity changed by $\delta v_{\phi,1}$ in the collision, then the collision contributes to the integral in equation (45) in the amount of

$$(\Delta t \Delta r)\delta \overline{F}_{\rm NL} = (r_1 - r_2)r_1 \delta v_{\phi,1} \qquad (46)$$

$$\approx r(r_1 - r_2)(\delta v_{\phi,1} - \delta v_{\phi,2})/2. \qquad (47)$$

To obtain the latter symmetric form, we approximated $r_1 \approx r$ and $\delta v_{\phi,1} \approx -\delta v_{\phi,2}$ (when in fact $r_1 \delta v_{\phi,1} = -r_2 \delta v_{\phi,2}$). The error accrued is of order $(r_1 - r_2)/r \sim s/r \ll 1$, where s is the particle size.

Since the number of collisions per unit time per unit radius is $n/2t_{\rm col}$,

$$\overline{F}_{r\phi} = \frac{n}{2t_{\rm col}} \frac{2r}{\Omega} \left\langle \delta\left(v_\phi^2\right) \right\rangle_c, \qquad (48)$$

$$\overline{F}_{\rm NL} = \frac{n}{2t_{\rm col}} \frac{r}{2} \left\langle (r_1 - r_2)\delta(v_{\phi,1} - v_{\phi,2}) \right\rangle_c, \qquad (49)$$

where $\langle \ \rangle_c$ (not to be confused with $\langle \ \rangle$) is an average over collisions and $\langle \delta(v_\phi^2) \rangle_c \equiv \langle \delta(v_{\phi,1}^2 + v_{\phi,2}^2) \rangle_c/2$. With our collision algorithm, $t_{\rm col}$ may be pulled out of the averages. We use equations (48) and (49) to extract $\overline{F}_{r\phi}$ and $\overline{F}_{\rm NL}$ from the simulations (see Fig. 8 below).

We can estimate the magnitudes of the two fluxes as follows. Since the peculiar velocity distribution is anisotropic, with $\langle v_\phi^2 \rangle = \langle v_r^2 \rangle/4 < \langle v_r^2 \rangle$ (eqs. [39]–[40]), and since collisions tend to isotropize the distribution, collisions systematically increase v_ϕ^2 by $\langle \delta(v_\phi^2) \rangle_c \sim v^2 \sim + e_{\rm rms}^2 (r\Omega)^2$, transporting $F_{r\phi}$ outwards. The contribution to $F_{\rm NL}$ is $\langle (r_1 - r_2)\delta(v_{\phi,1} - v_{\phi,2}) \rangle_c \sim +\Omega s^2$, where s is the particle size. This is true even when $e_{\rm rms} \gg s/r$ (i.e., when $\epsilon \to \epsilon_*$), because in that case $\delta(v_{\phi,1} - v_{\phi,2})$ is nearly random and hence nearly uncorrelated with $r_1 - r_2$. But because of the mean Keplerian shear, a small correlation $\sim \Omega s^2$ persists. This contribution also transports angular momentum outward. In sum,

$$\overline{F}_{r\phi} \sim r\Omega \frac{n}{t_{\rm col}}(re_{\rm rms})^2, \qquad (50)$$

$$\overline{F}_{\rm NL} \sim r\Omega \frac{n}{t_{\rm col}} s^2. \qquad (51)$$

6.3.1. Relating $n\dot{\mathcal{E}}$ to $F_H^{\rm visc}$

We now calculate the energy lost in an inelastic collision and thereby re-derive equation (24) from a microscopic perspective. Consider the collision of two particles having total velocities $\boldsymbol{V}_{1,2} = \boldsymbol{v}_{1,2} + \boldsymbol{V}_{1,2}^{\rm circ}$, where $\boldsymbol{V}_{1,2}^{\rm circ} = \Omega(r_{1,2})r_{1,2}\hat{\boldsymbol{\phi}}$ is the circular Keplerian speed at the positions of the particles. Then the specific energy lost per collision is, in previous notation,

$$(\Delta t \Delta r)\delta\left(\overline{n\dot{\mathcal{E}}}\right) = -\delta\left(V_1^2 + V_2^2\right)/2 \qquad (52)$$

$$= -\delta\left(v_1^2 + v_2^2\right)/2$$
$$- \delta\boldsymbol{v}_1 \cdot \boldsymbol{V}_1^{\rm circ} - \delta\boldsymbol{v}_2 \cdot \boldsymbol{V}_2^{\rm circ} \qquad (53)$$

$$= -\delta\left(v_1^2 + v_2^2\right)/2$$
$$- (r_1 - r_2)r_1 \delta v_{\phi,1}\, d\Omega/dr \qquad (54)$$

$$\approx -\delta\left(v_1^2 + v_2^2\right)/2$$
$$- (r_1 - r_2)r(d\Omega/dr)$$
$$\times \left(\delta v_{\phi,1} - \delta v_{\phi,2}\right)/2, \qquad (55)$$

where to derive equation (54) we used conservation of orbital angular momentum in a collision ($r_1 \delta v_{\phi,1} = -r_2 \delta v_{\phi,2}$). Therefore

$$\overline{n\dot{\mathcal{E}}} = -\frac{n}{2t_{\rm col}} \left\langle \delta(v^2) + \frac{r}{2}\frac{d\Omega}{dr}(r_1 - r_2)\delta(v_{\phi,1} - v_{\phi,2}) \right\rangle_c. \qquad (56)$$

We rewrite the first term using $v^2 = -3v_\phi^2 + e^2(r\Omega)^2$ (eqs. [39]–[40]). Since the particles are in collisional equilibrium,

$$\left\langle \delta(e^2) \right\rangle_c = 0, \qquad (57)$$

which implies that $\langle \delta(v^2) \rangle_c = -3\langle \delta(v_\phi^2) \rangle_c$. Inserting this into equation (56) and comparing the result with equations (48)–(49) completes our proof of equation (24).

6.3.2. Calculating $F_{r\phi}$ and ϵ_*

We calculate the numerical constant that we dropped in equation (50) and then use that result to calculate ϵ_*. Goldreich & Tremaine (1978) perform a similar calculation, with a different (although still idealized) collisional cross section. Shukhman (1984) accounts for $F_{\rm NL}$ as well. The treatments of Goldreich & Tremaine (1978) and Shukhman (1984) are more rigorous than ours, as they integrate over the velocity distribution function. They also consider the more general case of disks with order-unity optical depth. But their final expressions are "extremely cumbersome" (Shukhman 1984). Although our treatment is not rigorous, it is considerably simpler, and we justify it by comparing with simulations. We neglect $F_{\rm NL}$ in the present subsection, taking $e_{\rm rms} \gg s/r$.

For $\overline{F}_{r\phi}$ (eq. [48]), we seek

$$\left\langle \delta\left(v_\phi^2\right) \right\rangle_c = \left\langle v_\phi^2 \right\rangle_{\rm ac} - \left\langle v_\phi^2 \right\rangle_{\rm bc}, \qquad (58)$$

where $\langle \ \rangle_{\rm bc}$ is an average over collisions of the state immediately before the collision and $\langle \ \rangle_{\rm ac}$ is of the state immediately after. In an optically thin disk, the averages over particles are equal to time averages for a single particle:

$$\left\langle v_r^2 \right\rangle = \frac{e_{\rm rms}^2}{2}(r\Omega)^2, \quad \left\langle v_\phi^2 \right\rangle = \frac{e_{\rm rms}^2}{8}(r\Omega)^2, \qquad (59)$$

using equations (39)–(40). With our collision algorithm, the probability that a particle collides is uniform in time. Therefore

$$\left\langle v_{(r,\phi)}^2 \right\rangle_{\rm bc} = \left\langle v_{(r,\phi)}^2 \right\rangle. \qquad (60)$$

In collisional equilibrium (eq. [57]),

$$\left\langle \delta\left(v_r^2 + 4v_\phi^2\right) \right\rangle_c = 0. \qquad (61)$$

We now evaluate $\langle v_r^2 \rangle_{\rm ac}$ and $\langle v_\phi^2 \rangle_{\rm ac}$. We make the plausible assumption that the relative velocity of collision partners,[8] $\boldsymbol{u} = \boldsymbol{v}_1 - \boldsymbol{v}_2$, is isotropically distributed after the collision:

$$\left\langle u_r^2 \right\rangle_{\rm ac} = \left\langle u_\phi^2 \right\rangle_{\rm ac}. \qquad (62)$$

---

[8] Since we take $e \gg s/r$, we neglect the difference in the Keplerian circular velocities at the positions of the two particles.

This assumption is verified by numerical simulation in § 6.4. We relate $\boldsymbol{u}$ to $\boldsymbol{v}$ with

$$\left\langle u^2_{(r,\phi)} \right\rangle_{\rm bc} = 2 \left\langle v^2_{(r,\phi)} \right\rangle_{\rm bc}, \tag{63}$$

$$\left\langle \delta\left(u^2_{(r,\phi)}\right) \right\rangle_c = 4 \left\langle \delta\left(v^2_{(r,\phi)}\right) \right\rangle_c. \tag{64}$$

For the first relation, we neglected the correlation between $\boldsymbol{v}_1$ and $\boldsymbol{v}_2$ before a collision, and for the second relation, we used $\delta(\boldsymbol{v}_1 + \boldsymbol{v}_2) = 0$. Equations (62)–(64) yield $\langle \delta(v^2_\phi - v^2_r) \rangle_c = (1/2)\langle v^2_r - v^2_\phi \rangle_{\rm bc}$, which, with equations (59)–(61), becomes

$$\left\langle \delta\left(v^2_\phi\right) \right\rangle_c = \frac{3}{80} e^2_{\rm rms} (r\Omega)^2, \tag{65}$$

giving the numerical constant for $\overline{F}_{r\phi}$ (eq. [48]).

To calculate ϵ_*, we evaluate the specific energy lost per collision in the center-of-mass frame:

$$-\frac{1}{4} \left\langle \delta(u^2) \right\rangle_c = \frac{9}{80} e^2_{\rm rms}(r\Omega)^2, \tag{66}$$

(eqs. [62], [65], and [66]). We can also evaluate the energy loss as follows: from equation (3), it is

$$\frac{1}{4}\left(1 - \epsilon^2\right)\left\langle u^2_{\rm rel,\|} \right\rangle_{\rm bc} = \left(1 - \epsilon^2\right)\frac{1}{8}\left\langle u^2 \right\rangle_{\rm bc}, \tag{67}$$

where we have made use of the isotropy of the precollision $\boldsymbol{u}$ with respect to the axis connecting the centers of the two particles. Since $\langle u^2 \rangle_{\rm bc} = (5/4)e^2_{\rm rms}(r\Omega)^2$, equations (66) and (67) are equal only if ϵ is equal to

$$\epsilon_* = \sqrt{7}/5 = 0.529. \tag{68}$$

This is interpreted as the one value for ϵ that enables the velocity distribution to equilibrate in the limit that $e_{\rm rms} \gg s/r$, i.e., $F_{r\phi} \gg F_{\rm NL}$.

6.4. Dynamics from a Microscopic Perspective: Simulations

In Figure 8 we test the theoretical results derived in § 6.3. In the top panel, for the simulation with the same initial conditions as the one with $\epsilon = 0.525$ in Figures 2 and 7, we compute $\langle \delta(v_\phi)^2 \rangle_c$—the key factor that enters into $F_{r\phi}$ (eq. [48])—in two ways: first as an average over all particles that collide within successive time intervals of 2000 yr, and second using equation (65), where $e^2_{\rm rms} = \langle e^2 \rangle$ is a spatial, not temporal, average over all particles (regardless of whether they collide). The agreement verifies equation (65). Also shown in the top panel is the corresponding contribution to $F_{\rm NL}$, i.e., $(\Omega/4)\langle(r_1 - r_2)\delta(v_{\phi,1} - v_{\phi,2})\rangle_c$ (eq. [49]). That this quantity is constant with time and sits far below $\langle\delta(v_\phi)^2\rangle_c$ is expected from equations (50)–(51), given this simulation in which $e_{\rm rms} \gg s_{\rm grid}/\bar{r}$ (i.e., $\epsilon_* - \epsilon \ll \epsilon_*$).

In the bottom panel of Figure 8, we test our assumption, made in equation (62), that postcollision relative velocities are isotropic. The measured near-equality between $\langle u^2_r \rangle_{\rm ac}$ and $\langle u^2_\phi \rangle_{\rm ac}$ is satisfactory.

Finally, returning to Figure 7, we plot separately the contributions to the total energy dissipation from $F_{r\phi}$ and $F_{\rm NL}$. The former contribution is described by

$$k^{r\phi}_E \equiv \frac{-F_{r\phi}(d\Omega/dr)}{n^2 s^4_{\rm grid}(3\Omega^2/8 r t_{\rm orb})} \tag{69}$$
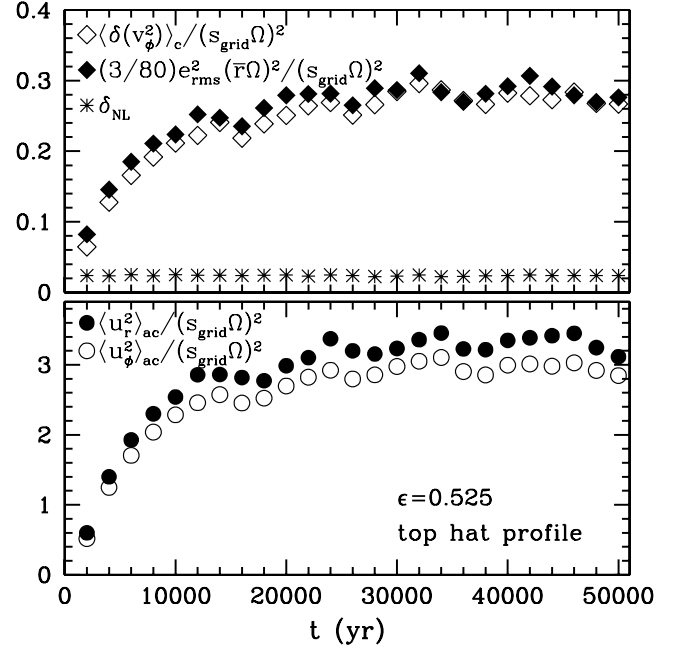

FIG. 8.—Averages over collisions. The two panels show the time evolution of various collisional averages in a simulation with the same initial conditions as the one with $\epsilon = 0.525$ in Figs. 2 and 7. *Top panel*: Open diamonds show the factor that enters into $F_{r\phi}$ (eq. [48]), i.e., $\langle\delta(v^2_\phi)\rangle_c = (1/2)\langle\delta(v^2_{\phi,1} + v^2_{\phi,2})\rangle_c$, normalized as shown. The averaging over collisions is done by recording the peculiar velocities of colliding particles immediately before and after each collision. The averaging time is 2000 yr. Filled diamonds give $e^2_{\rm rms} = \langle e^2 \rangle$ (a spatial, not temporal, average over all particles), multiplied by the appropriate prefactor as given by eq. (65). The agreement between open and filled diamonds confirms eq. (65). Stars give the nonlocal contribution, appropriately normalized relative to the open diamonds, i.e., $\delta_{\rm NL} \equiv (\Omega/4)\langle(r_1 - r_2)\delta(v_{\phi,1} - v_{\phi,2})\rangle_c/(s_{\rm grid}\Omega)^2$ (eqs. [48]–[49]). *Bottom panel*: Postcollision relative velocities are indeed nearly isotropic, as we had surmised in eq. (62). For this figure, we take $\boldsymbol{u} = \boldsymbol{V}_1 - \boldsymbol{V}_2$, the total relative velocity; it includes the difference in the circular Keplerian velocities at the locations of the two particles.

(see eqs. [24], [26], and [38]). We measure $F_{r\phi}$ according to

$$\overline{F}_{r\phi} \doteq \left(\frac{r}{\Omega}\right)\frac{\delta(v^2_\phi)_{>r_1} - \delta(v^2_\phi)_{>r_2}}{dt_m(r_1 - r_2)}, \tag{70}$$

where $\delta(v^2_\phi)_{>r}$ is the total change in v^2_ϕ summed over particles that collide between times t_m and $t_m + dt_m$, at radii $>r$. For simplicity, we evaluate $k^{\rm NL}_E = k_E - k^{r\phi}_E$.

7. SUMMARY AND OUTLOOK

We have introduced an algorithm to simulate collisions between inelastic particles in an optically thin disk orbiting a central mass. The algorithm is simple to implement and adds negligible running time to existing collisionless N-body codes. A major feature of the algorithm is that the disk particles' motions need only be tracked in a plane. Yet the algorithm transcends its two-dimensional appearance to simulate a three-dimensional disk of particles whose random velocity distribution tends to be isotropized by collisions.

We have performed a battery of tests of the algorithm for the case of an isolated, narrow, circular ring. Numerical simulations agree with analytic theory with regard to how the particles' velocity dispersion equilibrates, how the ring viscously spreads, how energy and angular momentum are transported, and how energy dissipation relates to the viscous angular momentum flux and to the background shear. Angular momentum transport arises not

only from particle advection (HF_n) but also from correlations in the random velocity field ($F_{r\phi}$) and from finite particle sizes (F_{NL}). The relative magnitudes of each of these three terms can be measured from simulations. In making these and other measurements, we sought ways to minimize noise introduced by finite particle numbers (Poisson fluctuations). For example, when measuring viscous fluxes of angular momentum and energy, it proves useful to consider only those particles that actually collide during the measurement interval.

The stage is now set for simulating more complicated systems: narrow eccentric rings (such as the Maxwell and Titan ringlets of Saturn or the ϵ ring of Uranus) and circumstellar disks with embedded planets. Among the phenomena we are interested in exploring numerically are the formation of sharp edges by shepherd satellites, the evolution of narrow rings into states of rigid apsidal precession, and the eccentricity evolution of planets as driven by disks.

APPENDIX: ON REALISTIC PARTICLE SIZES

In this paper, we do not simulate gravitational interactions between test particles. Collisions among *massless* particles maintain their relative eccentricities at $\sim s_{grid}/r$ (eq. [4]). But massive particles with material density ρ and radius $s_{massive}$ excite their relative speeds to the escape speed from their surfaces, $\sim (G\rho)^{1/2} s_{massive}$ (e.g., Goldreich et al. 2004, and references therein). The corresponding eccentricity is $\sim (s_{massive}/r)(r/R_\odot)^{3/2}$, where $R_\odot$ is the Sun's radius, and we have used the fact that the Sun's density is comparable to that in solid bodies. Thus, for example, massless particles with $r = 1$ AU and $s_{grid} = 0.001$ AU $= 150,000$ km (the conditions we use in our simulations) excite themselves to the same eccentricities as do massive particles of size $s_{massive} \sim s_{grid}(R_\odot/r)^{3/2} \sim 50$ km. In a disk with massive particles of size $s_{massive}$ that stir themselves, the collision time is clearly the same as in a disk of massless particles of the same size. But the argument leading to equation (9) now gives for the diffusion time $t_{diff} \sim t_{col}(\Delta/s_{massive})^2(R_\odot/r)^3$. In sum, care must be used when applying results from simulations of massless particles, and one cannot simply replace s_{grid} with $s_{massive}$.

REFERENCES

Brahic, A. 1977, A&A, 54, 895
Charnoz, S., Thébault, P., & Brahic, A. 2001, A&A, 373, 683
Chiang, E. I., & Culter, C. J. 2003, ApJ, 599, 675
Goldreich, P., Lithwick, Y., & Sari, R. 2004, ARA&A, 42, 549
Goldreich, P., & Sari, R. 2003, ApJ, 585, 1024
Goldreich, P., & Tremaine, S. D. 1978, Icarus, 34, 227
Greenberg, R. 1988, Icarus, 75, 527
Levison, H. F., & Duncan, M. J. 1994, Icarus, 108, 18
Lewis, M. C., & Stewart, G. R. 2000, AJ, 120, 3295
Lynden-Bell, D., & Pringle, J. E. 1974, MNRAS, 168, 603
Petit, J.-M., & Henon, M. 1987, A&A, 188, 198
Press, W. H., Teukolsky, S. A., Vetterling, W. T., & Flannery, B. P. 1992, Numerical Recipes in FORTRAN: The Art of Scientific Computing (2nd ed.; Cambridge: Univ. Press)
Shukhman, I. G. 1984, Soviet Astron., 28, 574
Thommes, E. W., Duncan, M. J., & Levison, H. F. 2003, Icarus, 161, 431
Trulsen, J. 1971, Ap&SS, 12, 329
Wisdom, J., & Holman, M. 1991, AJ, 102, 1528
Wisdom, J., & Tremaine, S. 1988, AJ, 95, 925